

An optimized smearing scheming for first Brillouin zone sampling and its application on thermal conductivity prediction of graphite

Chengye Li(李承业), Changying Zhao(赵长颖), and Xiaokun Gu(顾骁坤)
Citation: Chin. Phys. B, 2023, 32 (**6**): 064401. DOI: 10.1088/1674-1056/ac9223
Journal homepage: http://cpb.iphy.ac.cn; http://iopscience.iop.org/cpb

What follows is a list of articles you may be interested in

Thermal transport properties of two-dimensional boron dichalcogenides from a first-principles and machine learning approach

Zhanjun Qiu(邱占均), Yanxiao Hu(胡晏箫), Ding Li(李顶), Tao Hu(胡涛), Hong Xiao(肖红),Chunbao Feng(冯春宝), and Dengfeng Li(李登峰)
Chin. Phys. B, 2023, 32 (**5**): 054402. DOI: 10.1088/1674-1056/acb9e6

Modeling of thermal conductivity for disordered carbon nanotube networks

Hao Yin(殷浩), Zhiguo Liu(刘治国), and Juekuan Yang(杨决宽)
Chin. Phys. B, 2023, 32 (**4**): 044401. DOI: 10.1088/1674-1056/acb0be

Accurate prediction of the critical heat flux for pool boiling on the heater substrate

Fengxun Hai(海丰勋), Wei Zhu(祝薇), Xiaoyi Yang(杨晓奕), and Yuan Deng(邓元)
Chin. Phys. B, 2022, 31 (**6**): 064401. DOI: 10.1088/1674-1056/ac523c

Construction and mechanism analysis on nanoscale thermal cloak by *in-situ* annealing silicon carbide film

Jian Zhang(张健), Hao-Chun Zhang(张昊春), Zi-Liang Huang(黄子亮), Wen-Bo Sun(孙文博), and Yi-Yi Li(李依依)
Chin. Phys. B, 2022, 31 (**1**): 014402. DOI: 10.1088/1674-1056/ac2809

First-principles analysis of phonon thermal transport properties of two-dimensional WS_2/WSe_2 heterostructures

Zheng Chang(常征), Kunpeng Yuan(苑昆鹏), Zhehao Sun(孙哲浩), Xiaoliang Zhang(张晓亮), Yufei Gao(高宇飞), Xiaojing Gong(弓晓晶), and Dawei Tang(唐大伟)
Chin. Phys. B, 2021, 30 (**3**): 034401. DOI: 10.1088/1674-1056/abd2a6

An optimized smearing scheming for first Brillouin zone sampling and its application on thermal conductivity prediction of graphite

Chengye Li(李承业)[1], Changying Zhao(赵长颖)[1,2], and Xiaokun Gu(顾骁坤)[2,†]

[1] *China-UK Low Carbon College, Shanghai Jiao Tong University, Shanghai* 200240, *China*
[2] *School of Mechanical Engineering, Shanghai Jiao Tong University, Shanghai* 200240, *China*

(Received 30 April 2022; revised manuscript received 9 September 2022; accepted manuscript online 15 September 2022)

We propose an optimized scheme to determine the smearing parameter in the Gaussian function that is used to replace the Dirac δ function in the first Brillouin zone sampling. The broadening width is derived by analyzing the difference of the results from the phase-space method and Gaussian broadening method. As a demonstration, using the present approach, we investigate the phonon transport in a typical layered material, graphite. Our scheme is benchmarked by comparing with other zone sampling methods. Both the three-phonon phonon scattering rates and thermal conductivity are consistent with the prediction from the widely used tetrahedron method and adaptive broadening method. The computational efficiency of our scheme is more than one order of magnitude higher than the two other methods. Furthermore, the effect of four-phonon scattering in phonon transport in graphite is also investigated. It is found that four-phonon scattering reduces the through-plane thermal conductivity by 10%. Our methods could be a reference for the prediction of thermal conductivity of anisotropic material in the future.

Keywords: graphite, thermal conductivity, phonon transport, Boltzmann transport equation

PACS: 44.10.+I, 63.20.kg, 66.70.–f, 81.05.uf **DOI:** 10.1088/1674-1056/ac9223

1. Introduction

The first-principles-based phonon Boltzmann transport equation (PBTE) has become dominant in predicting thermal properties of solids in past decade.[1–4] The key step of this approach is to perform the first Brillouin zone (FBZ) integration to sum up the scattering rates of all possible phonon scattering events. The FBZ is usually firstly discretized into uniform $\boldsymbol{q}$-point grids and then the rates of scatterings of the phonons on the grid are computed through Fermi's golden rule,[5] in which the Dirac δ function appears to ensure the conservation of energy before and after the scattering. To deal with the Dirac δ function in FBZ integration, the sampling methods adopted in PBTE calculations typically fall within one of the two categories: analytical methods[6–9] and finite-width function methods.[10–13] The typical analytical methods include the phase space approach[7,8] or tetrahedron method.[6,9,14] The basic idea is to approximate the integrand and phonon frequency as a linear function of the wave vector so that the Dirac δ function can be analytically treated by reducing the dimension of integration. Since such an approximation needs the frequency information of neighboring phonon modes on the same branch, it becomes challenging for crystals with complicated structures, as crossing of phonon branches occasionally occurs requiring additional efforts on sorting phonon modes at each wave vector.[7] The finite-width function methods replace the Dirac δ function with a simple continuous function, such as the Gaussian and Lorentzian functions,[9,10,13,15] which became popular since the FBZ integration can be performed numerically directly and one does not need to handle the crossing of phonon branches purposefully. However, the scattering rates calculated by the finite-width function methods are significantly affected by the corresponding smearing scheme. Both fixed and adaptive smearing parameters are adopted. The most popular adaptive scheme, which employs some open-sourced PBTE packages,[15] is to determine the broadening width based on the information of the phonon group velocities and the space between neighboring $\boldsymbol{q}$-points along the directions of three reciprocal vectors. For layered crystals, such as graphite, the frequency difference between neighboring phonons are quite distinct along various directions, thus it is unclear to how to rationally determine the broadening width. In literatures, some authors had noticed that different FBZ sampling methods could lead to distinct thermal conductivity values. For instance, Lindsay *et al.*[16] found that there are a 8% deviation when applying the phase space approach and the finite-width function method to calculate the thermal conductivity of graphene. Considering that the computed phonon scattering rates are highly relevant to the accuracy of the thermal conductivity prediction, it is necessary to explore the influence of the FBZ sampling methods on the phonon scattering prediction and to uncover the underlying mechanisms.

The recent measurements[17–19] and theoretical calculations[20–24] showed that four-phonon scattering is critical phonon scattering mechanism for a few materials in a wide temperature range. Due to the demanding computational requirement,[25] whether four-phonon scattering is important

†Corresponding author. E-mail: xiaokun.gu@sjtu.edu.cn

© 2023 Chinese Physical Society and IOP Publishing Ltd

has not been investigated for most materials yet. A good smearing scheme along with the finite-width method on FBZ integration is beneficial to solve this issue, as a properly chosen broadening width could not only be as small as possible to ensure minimum number of scattering events to be computed but also retain the accuracy of the integration.

In this paper, we present an optimized Gaussian broadening scheme for the finite-width function method. The broadening width is determined by examining the integration result from both the phase-space method and Gaussian broadening method. To validate the presented method and evaluate its performance we investigate the phonon scattering in bulk graphite. As the most representative layered material, the thermal conductivity of graphite had been intensively investigated several decades ago, but the theoretical prediction data on the through-plane direction in literature is rather scattered.[26–34] We compare the predicted phonon scattering rates and thermal conductivity with those from the analytical tetrahedron method and adaptive Gaussian method. Our optimized scheme is found to boost the computational efficiency by around 20 to 30 times in three-phonon and four-phonon calculation compared with the adaptive Gaussian method. We further discuss the influence of four-phonon scattering on the thermal conductivity of graphite.

2. BTE approach and FBZ sampling methods

Firstly, we briefly introduce the PBTE method to predict the thermal conductivity in Subsection 2.1, followed by a mini review on the mainstreaming schemes of the FBZ sampling used in phonon scattering rate calculations in Subsection 2.2. In Subsection 2.3, we derive the optimized broadening width of the Gaussian function that reproduces the correct values of the FBZ integration. Details on the first-principles calculations are presented in Subsection 2.4.

2.1. BTE and phonon scattering calculation

The lattice thermal conductivity tensor elements, $\kappa^{\alpha\beta}$, can be expressed as

$$\kappa^{\alpha\beta} = \frac{1}{\Omega}\sum_{\lambda}\hbar\omega_{\lambda}v_{\lambda}^{\alpha}n_{\lambda}^{0}\left(n_{\lambda}^{0}+1\right)F_{\lambda}^{\beta}, \tag{1}$$

where $\hbar$ is the reduced Planck constant, Ω is the volume of the unit cell, ω_{λ}, v_{λ}^{α} and n_{λ}^{0} are the phonon frequency, group velocity along the α direction and equilibrium phonon distribution function, respectively. F_{λ}^{β} is known as the deviation function, as $n_{\lambda}^{0}\left(n_{\lambda}^{0}+1\right)F_{\lambda}^{\beta}$ means the ratio between the nonequilibrium phonon population normalized by the small temperature gradient along the β direction that results in the heat flux. Equation (1) summates all phonon mode $\lambda=(\boldsymbol{q},s)$ over the FBZ, where $\boldsymbol{q}$ and s are the phonon wave vector and branch index, respectively. While the phonon frequency, group velocity and distribution function are determined by the phonon dispersion relation that is calculated by using the harmonic force constants as inputs, the mode-specific deviation function is extracted by solving the PBTE, which is written as

$$\nabla T\cdot v_{\lambda}^{\alpha}\frac{\partial F_{\lambda}}{\partial T} = W_{\lambda}^{\mathrm{3ph}}+W_{\lambda}^{\mathrm{4ph}}+W_{\lambda}^{\mathrm{isotope}}. \tag{2}$$

The right-hand side scattering term of PBTE in this work includes the three-phonon, four-phonon and phonon-isotope scattering terms. The three-phonon and four-phonon scattering terms are expressed as

$$W_{\lambda}^{\mathrm{3ph}} = \sum_{\lambda'}\sum_{\lambda''}\frac{2\pi}{\hbar}\left|\langle f|\Phi_3|i\rangle\right|^2\delta\left(E_f-E_i\right), \tag{3a}$$

$$W_{\lambda}^{\mathrm{4ph}} = \sum_{\lambda'}\sum_{\lambda''}\sum_{\lambda'''}\frac{2\pi}{\hbar}\left|\langle f|\Phi_4|i\rangle\right|^2\delta\left(E_f-E_i\right), \tag{3b}$$

where f and i denote the final and initial states, the δ function ensures energy conservation, Φ_3 and Φ_4 are the third- and fourth-order anharmonic terms of the potential energy under the normal mode representation, which result in phonon scatterings among three and four phonons, respectively. Equation (3a) represents the three-phonon processes $\boldsymbol{q}s\pm\boldsymbol{q}'s'\rightarrow\boldsymbol{q}''s''$, and Eq. (3b) represents the four-phonon processes $\boldsymbol{q}s\pm\boldsymbol{q}'s'\pm\boldsymbol{q}''s''\rightarrow\boldsymbol{q}'''s'''$.

2.2. Sampling method and integral on FBZ

The Dirac δ function in Eqs. (3a) and (3b) ensures the energy conservation before and after the scattering,

$$\begin{aligned}&\omega_{\lambda}\pm\omega_{\lambda'}-\omega_{\lambda''}=0,\\ &\omega_{\lambda}\pm\omega_{\lambda'}\pm\omega_{\lambda''}-\omega_{\lambda'''}=0.\end{aligned} \tag{4}$$

By using the momentum conservation condition, that is, $\boldsymbol{q}''$ can be expressed as the function of $\boldsymbol{q}$, $\boldsymbol{q}'$ and $\boldsymbol{q}'''$, and treating $\boldsymbol{q}'$ as a continuous variable, the summation over all possible three-phonon and four-phonon scattering events in the FBZ have the forms

$$I_{\mathrm{3ph}}^{\boldsymbol{q}s} = \sum_{s'}\sum_{s''}\int_{\Omega_{\mathrm{FBZ}}}\phi_{\mathrm{3ph}}\left(\boldsymbol{q}'\right)\delta\left(\omega_{\boldsymbol{q}'s'}-W_{\mathrm{3ph}}\right)\mathrm{d}\boldsymbol{q}', \tag{5a}$$

$$I_{\mathrm{4ph}}^{\boldsymbol{q}s} = \sum_{\boldsymbol{q}'''s'''}\sum_{s'}\sum_{s''}\int_{\Omega_{\mathrm{FBZ}}}\phi_{\mathrm{4ph}}\left(\boldsymbol{q}'\right)\delta\left(\omega_{\boldsymbol{q}'s'}-W_{\mathrm{4ph}}\right)\mathrm{d}\boldsymbol{q}', \tag{5b}$$

where ϕ_{3ph} and ϕ_{4ph} are simplified functions with respect to $\boldsymbol{q}'$, W_{3ph} and W_{4ph} are from the energy conservation conditions, that is, $W_{\mathrm{3ph}}=\omega_{\boldsymbol{q}''s''}\mp\omega_{\boldsymbol{q}s}$ and $W_{\mathrm{4ph}}=\omega_{\boldsymbol{q}'''s'''}\mp\omega_{\boldsymbol{q}s}\mp\omega_{\boldsymbol{q}''s''}$. The summations on s' and s'' in Eq. (5b) have the same form as Eq. (5a), both of which can be expressed as integrals with the same form

$$I=\int_{\Omega_{\mathrm{FBZ}}}\phi\left(\boldsymbol{q}'\right)\delta\left(\omega_{\boldsymbol{q}'s'}-W\left(\boldsymbol{q}'\right)\right)\mathrm{d}\boldsymbol{q}'. \tag{6}$$

Since $\boldsymbol{q}$ and $\boldsymbol{q}'''$ are fixed when evaluating the integral, Eq. (6), and $\boldsymbol{q}''$ are determined from the momentum conservation condition, and W ($W_{3\mathrm{ph}}$ or $W_{4\mathrm{ph}}$) is the function of $\boldsymbol{q}'$ only. There are two classes of methods that are commonly used to process the integral with δ function: the analytical method and finite-width function treatment.

2.2.1. Analytical method

The phase space method[7,8] and the tetrahedron method[6,9,14] belong to the analytical method, whose basic idea is to reduce the difficulty of Eq. (6) by converting the FBZ integration into simpler integration on a line or a volume fraction.

Take three-phonon scattering as an example. In the phase space method, the integral for mode $\boldsymbol{q}s$ can be computed as the following. Given the branch indices s' and s'', the modes $\boldsymbol{q}'s'$ and $\boldsymbol{q}''s''$ that interact with $\boldsymbol{q}s$ have to satisfy three momentum conservation conditions, leading to three constraint equations in a 6-dimensional $(\boldsymbol{q}', \boldsymbol{q}'')$ momentum space. Hence, only q'_x, q'_y and q'_z need to be concerned. Furthermore, for each (q'_x, q'_y), q'_z can be determined by the energy conservation condition through a direct root-finding scheme. Then, the integral is expressed as

$$I(W) = \sum_{\boldsymbol{q}'_i} \frac{\phi(\boldsymbol{q}'_i)}{\left| \dfrac{\partial\left(\omega_{\boldsymbol{q}'s'} - W(\boldsymbol{q}')\right)}{\partial q'_z} \right|_{\omega_{\boldsymbol{q}'s'} - W(\boldsymbol{q}') = 0}}, \tag{7}$$

where the summation is over the wave vectors at which the mode $\boldsymbol{q}'_i s'$ fulfills the condition $\omega_{\boldsymbol{q}'_i s'} = W(\boldsymbol{q}')$. When using the phase space method, one needs to check the eigenvector and frequency information of phonons to make sure the root-finding is performed on the same phonon branch, as crossing of phonon branches commonly occurs in crystals with complicated structure.[7]

In the tetrahedron method, assuming ϕ and ω to be linear with respect to $\boldsymbol{q}$, the FBZ is decomposed into a few tetrahedrons with the same volume. The space integral of a tetrahedron can be transformed into surface integral of the triangle intersecting with the tetrahedron, and the integral $I(W)$ can be written as

$$I(W) = \sum_{m,n} r_m^n(W)\, \phi_n(\boldsymbol{q}_m), \tag{8}$$

where n and m denote the n-th tetrahedron and m-th corner point in a tetrahedron, $\phi_n(\boldsymbol{q}_m)$ indicates the function value of ϕ at the m-th corner point of the n-th tetrahedron, and $r_m^n(W)$ is the weight factor related to W. Similar to the phase space method, the tetrahedron method also requires extra computational process to ensure the modes on the corners of tetrahedrons are on the same branch.

2.2.2. Finite-width function method

Another class of numerical scheme to perform FBZ sampling in PBTE is to substitute the non-integrable δ function by a specific continuous finite-width function directly. Since the integrand is a continuous function after the substitution, the integral can be determined by simple numerical integration straightforwardly. One common choice is to use the Gaussian function[10,13,15] with a finite width σ,

$$G(\omega_{\boldsymbol{q}} - W) = \frac{1}{\sqrt{\pi}\sigma} \mathrm{e}^{-\frac{(\omega_{\boldsymbol{q}} - W)^2}{\sigma^2}}. \tag{9}$$

In some literatures,[10,15] a slightly different expression is used by replacing σ in Eq. (9) by $\sqrt{2}\sigma'$. It is desirable to use a σ as small as possible to approach the ideal δ function, but this could make phonons experience insufficient scatterings if σ is too small. On the other hand, a too large σ will make phonon scattering events that do not fulfill the energy conservation happen. Therefore, an optimal σ is the key to the accuracy of finite-width function.

Previously, many researchers used the fixed coefficient σ_{fixed} as the broadening width, which left the coefficient with artificial and arbitrary nature. For example, the results of diamond using σ_{fixed} shows numerical instability under small grid and has evident impact on the iteration times of BTE calculation.[13] The adaptive method of Gaussian function was firstly used to solve the problem of electron density and energy state in phase space,[35] then the sampling scheme was transplanted in some open-sourced package to calculate phonon scattering rates.[10,15,25] The recommended value of σ_{A} for three-phonon scattering by Li *et al.*[15] is expressed as

$$\begin{aligned} \sigma_{\mathrm{A}} &= \sqrt{2}\sigma'_{\mathrm{A}} = \sqrt{2} \cdot \sqrt{\sum_{\mu} \left(\frac{\partial W}{\partial q'^{\mu}}\right)^2 E\left\{\left(q'^{\mu} - q'^{\mu}_0\right)^2\right\}} \\ &\simeq \sqrt{2} \cdot \sqrt{\frac{1}{12}\sum_{\mu}\left[\sum_{\alpha}\left(v^{\alpha}_{\lambda'} - v^{\alpha}_{\lambda''}\right)\frac{\boldsymbol{Q}^{\alpha}_{\mu}}{N_{\mu}}\right]^2}, \end{aligned} \tag{10}$$

where $\boldsymbol{q}'^{\mu}$ is the projection of $\boldsymbol{q}'$ over reciprocal-space lattice vector $\boldsymbol{Q}_{\mu}$, $v^{\alpha}_{\lambda'}$ is the phonon velocity along axis α, and the function E is the mathematical expectation. The physical meaning of coefficient σ'_{A} provided by Li *et al.* is the statistical variance value of frequency along each component of $\boldsymbol{q}'$ in a mesh cell. If the frequency difference between neighboring $\boldsymbol{q}$ points is highly direction dependent, for example, $\sum_{\alpha}\left|\boldsymbol{Q}^{\alpha}_{\mu_1}\left(v^{\alpha}_{\lambda'} - v^{\alpha}_{\lambda''}\right)/N_{\mu_1}\right| \gg \sum_{\alpha}\left|\boldsymbol{Q}^{\alpha}_{\mu_i}\left(v^{\alpha}_{\lambda'} - v^{\alpha}_{\lambda''}\right)/N_{\mu_i}\right|$, $(i = 2, 3)$, the broadening width according to Eq. (10) could be too large for the directions $\boldsymbol{Q}_{\mu_2}$ and $\boldsymbol{Q}_{\mu_3}$, as it covers many $\boldsymbol{q}$-points that the energy conservation condition is not fulfilled. Hence, this choice of the broadening width treats the three directions equally, which may produce unsatisfactory results for some highly anisotropic materials.

2.3. Optimized method for δ function approximation

Being aware of that the analytical method is parameter free while the finite-width function method avoids dealing with the phonon branch crossing, we propose a method combining the advantages of them, which is suitable for the case of materials with strong anisotropy. The main procedures of the phase-space method are firstly to perform the integration in one dimension, where the Dirac δ function is treated analytically, and then to conduct summation on the other two directions. Following this idea, we firstly derive the expression for the broadening width σ_{E} of the Gaussian function that can lead to the correct result on one-dimension integration.

We assume ϕ and ω are linear with respect to $\boldsymbol{q}$ on one-dimensional uniformly distributed q-points, and the point, $\tilde{q}$, that satisfies the energy conversation, is located between two points, q_i and q_{i+1}, and the integral value is

$$\begin{aligned} I_1 &= \frac{\phi(\tilde{q})}{\left|\frac{\partial\omega}{\partial q}|_{q=\tilde{q}}\right|} \simeq \frac{p_0\phi(q_i)+p_1\phi(q_{i+1})}{\left|\frac{\omega(q_{i+1})-\omega(q_i)}{\Delta q}\right|} \\ &= \Delta q[(\omega(q_{i+1})-W)\phi(q_i) \\ &\quad +(W-\omega(q_i))\phi(q_{i+1})], \end{aligned} \tag{11}$$

where $\Delta q = q_{i+1}-q_i$, $p_0 = (\omega(q_{i+1})-W)/(\omega(q_{i+1})-\omega(q_i))$ and $p_1 = (W-\omega(q_i))/(\omega(q_{i+1})-\omega(q_i))$.

Meanwhile, based on the trapezoidal rule of numerical integration, the integral value can be approximated by the information of the two points, if $\tilde{q}$ is in between, as

$$\begin{aligned} I_2 \simeq \frac{1}{2}&[\phi(q_i)G(\omega(q_i)-W) \\ &+\phi(q_{i+1})G(\omega(q_{i+1})-W)]\Delta q, \end{aligned} \tag{12}$$

where we further assume that $\phi(\boldsymbol{q})$ is a constant function. According to the dimensional analysis on the equality $I_1 \simeq I_2$, the broadening coefficient has to be expressed as $\sigma_{\mathrm{E}} = a|v|\Delta q = a|\omega_1-\omega_0|$, where a is a coefficient. ω_0 is the frequency satisfying $\omega(q)=W$ and $|\omega_1-\omega_0|$ is equal to $\Delta\boldsymbol{q}$ multiplying phonon group velocity $|v|$. Therefore, the Gaussian function coefficient σ_{E} is directly linked to the specific phonon scattering event and one can choose the optimum a that makes the numerical integration result be I_1.

When using the Gaussian function to perform the FBZ integration, all q-points are covered and the calculated integral is thus expressed as

$$\begin{aligned} I_3 &= \Delta q\sum_i \phi(q_i)G(\omega(q_i)-W) \\ &= \Delta q\sum_i \phi(q_i)\frac{1}{\sqrt{\pi}a|v|\Delta q}\mathrm{e}^{-\frac{(\omega(q_i)-W)^2}{(a|v|\Delta q)^2}}. \end{aligned} \tag{13}$$

Since $\tilde{q}$ is not necessary on the q-points but can be located in any location, we consider two extreme cases: the scattering happens 1) on the center of the two points (q_i, q_{i+1}) and 2) exactly on single point (q_i), which are illustrated in Fig. 1. The numerical results of the summation on the two cases are denoted as I_{3-1} and I_{3-2}, respectively. A good value of a should be capable of making I_{3-1} and I_{3-2} as close to I_1 as possible, simultaneously.

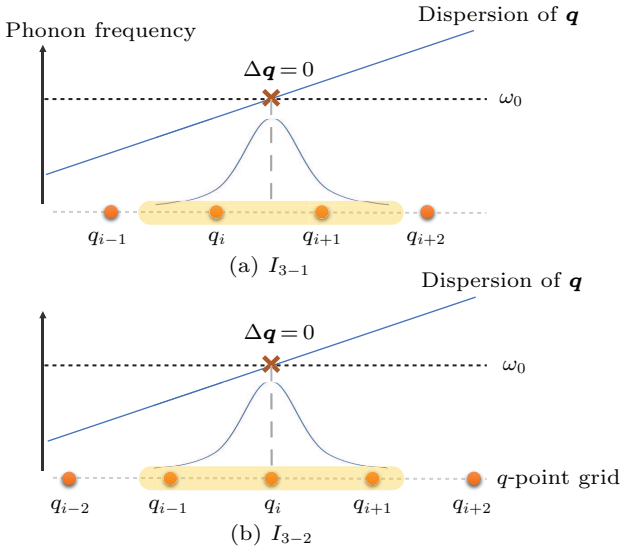


Fig. 1. Schematic diagram of Gaussian function sampling on 1-D q-point grid (ω_0 projection coordinates of intersection point siting at middle of two points or on one point).

The numerical values of I_{3-1} and I_{3-2} as a function of a are computed and shown in Fig. 2(a). I_{3-1} is found larger than the exact result I_1 while I_{3-2} is smaller for any finite a. However, as expected, these results of both cases converge to the exact solution, 1.0, if a is sufficiently large. In particular, when $a=0.6$, the deviation of I_{3-1} and I_{3-2} from I_1 is around 5.7%. Due to the cancellation of the deviations, the difference between I_1 and $\frac{1}{2}(I_{3-1}+I_{3-2})$ is negligible (less than 0.2%).

In practice, instead of dealing with all q-points in the FBZ, the number of summed items in Eq. (13) can be controlled by excluding the items that the frequency difference $|\omega(q_i)-W|$ is large. For the Gaussian broadening function, a reasonable cutoff is $|\omega(q_i)-W| > 2\sigma_{\mathrm{E}}$, as it can cover 99.5% of the area beneath the Gaussian function. By imposing such a cutoff, the error of I_{3-1} and I_{3-2} from I_1 is increased to some extent, as shown in Fig. 2(b), but $\frac{1}{2}(I_{3-1}+I_{3-2})$ is only 1.5% smaller than I_1, which confirms that our scheme, $\sigma_{\mathrm{E}} = 0.6|v|\Delta q$, along with the Gaussian function can reproduce the exact solution. The optimized broadening width along with the introduced cutoff minimizes the amount of phonon scattering events to be computed, as we find that for both of the two cases, only two or three points near each $\tilde{q}$ are sufficient to reproduce the correct result. Since our scheme ensures a good accuracy on one-dimensional integration with the Dirac δ function, one only needs to perform summation on the other two directions to obtain the results of the FBZ sampling in a three-dimensional space. We suggest that the direction with lower average phonon velocity $\boldsymbol{v}^{\mu}$ be selected as the integration direction of δ function, and the other two directions are used as the direction of summation. Compared with the

adaptive method, our optimized broaden coefficient is more intuitive and directly related to the phonons scattering condition, which are also simpler calculation formula compared with Eq. (7).

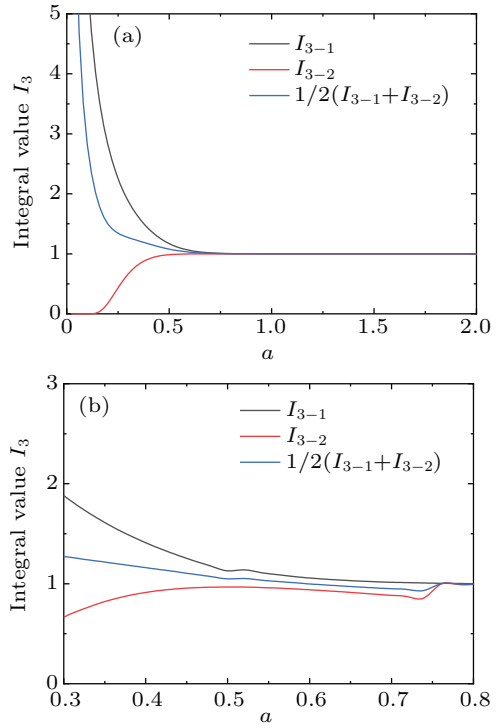


Fig. 2. The integration result as a function of the coefficient a (a) without imposing a cutoff; (b) with a cutoff.

2.4. Computational detail of graphite

To test our optimized scheme of FBZ sampling, we calculate the phonon scattering rates and predict the thermal conductivity of graphite. First-principles calculations are adopted to obtain the interatomic force constants of graphite as inputs for PBTE calculations.

For DFT calculations, we use QUANTUM ESPRESSO package[36] with standard local pseudopotential (LDA, GGA, PBE) and nonlocal correlation functional (vdW-DF[37] and rVV10[38]). The kinetic energy cutoff is chosen as 80 Ry and 24×24×12 Monkhorst–Pack k-point grids are used for structural minimization. In Table 1, we report the results of the optimized graphite lattice constants, a_0 and $c_0/2$ based on the ground energy state for all considered functionals, where the LDA and rVV10 calculations give lattice constants a_0 closer to experiments data (within 1%) than other vdW functionals. For the consistent lattice constant c_0, the optB88 and optB88vdW overestimate it by $\sim 3\%$ and LDA underestimates it by about 1%, while the rVV10 and vdW-DF2 are in good agreement with experimental data.[27,39–41] The results show that the LDA and functional correction can get relatively accurate description of the lattice structure, while it leads to some differences in the dispersion relation.

Figure 3(a) shows the dispersion of phonons obtained with LDA and vdW functionals rVV10 and vdW-DF2 comparing with experiment of inelastic x-ray scattering (IXS).[40–42] For the high-symmetry line Γ–K–M–Γ, all nonlocal functionals describe the phonon dispersion reasonably well, which is consistent with the characteristics of the experimental data. In Fig. 3(b), the LDA and vdW-DF2 tend to slightly underestimate the phonon frequencies in low frequency branches in Γ–A, which may lead to previously underestimated phonon contribution to thermal conductivity of graphite.[30] Based on the above discussion, we choose rVV10 in this work to generate the force constants for its satisfactory description of both the lattice constants and phonon dispersion.[38]

The force constants are extracted by fitting the force-displacement data in 5×5×4 supercells and use cutoffs of $2.5a_0$, $1.55a_0$ and $1.5a_0$ for the second, third and fourth-order force constants, respectively. To calculate the thermal conductivity, we solve the PBTE iteratively[4] along with the $\boldsymbol{q}$-point grid of $N_1 : N_2 : N_3 = 2 : 2 : 1$ on FBZ, which takes into account the lattice structure, comparable energy spacing and the limitation of computing power. And we chose the z direction of graphite to integrate δ function with lower average phonon speed.

Table 1. Lattice constants obtained by different VDW functional corrections.

Exchange correlation	Lattice constant a_0 (Å)	Lattice constant $c_0/2$ (Å)
LDA	2.469	3.120
optB88	2.485	3.465
optB88vdW	2.485	3.554
vdW-DF	2.490	3.345
rVV10	2.469	3.362
EXP[41]	2.46	3.356

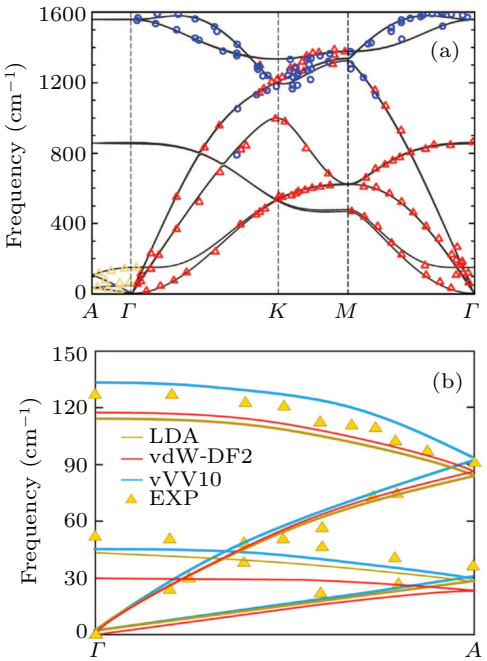


Fig. 3. (a) Comparison between phonon dispersion relation of graphite and experimental values (blue circles and red triangles are from Refs. [39,40], yellow triangles are from Ref. [38]) and (b) comparison between Γ–A phonon dispersion relation of graphite and experimental values.

3. Result and discussion

3.1. Influence of sampling methods on phonon transport properties

Figure 4 displays the three-phonon scattering rate of LA phonons along the chosen high symmetric path Γ–A in the FBZ. Dotted lines and solid lines represent the results calculated using two different $\boldsymbol{q}$-point grids ($N_1 = 16$ and $N_1 = 32$) based on three sampling methods (tetrahedron method, Gaussian method with adaptive and our optimized broadening schemes). The scattering rate of phonons near the Γ point increases rapidly with the wave vector. With the further increase of the wave vector, the scattering rate reaches the maximum and then slowly decreases to around 2.5×10^{-5} ps^{-1}. It can be clearly seen that the scattering rates from different sampling methods have a considerable deviation with each other when $N_1 = 16$, but the results seem more converged as increasing the $\boldsymbol{q}$-points density to $N_1 = 32$. As the analytical tetrahedron method is regarded as a standard approach for FBZ sampling, to evaluate the accuracy of our Gaussian broadening scheme, we define an error value $\varepsilon_{\boldsymbol{q}} = \frac{\mathrm{SR}_{\boldsymbol{q}}}{\mathrm{SR}^0_{\boldsymbol{q}}} \times \frac{\mathrm{SR}_{\boldsymbol{q}}}{\sum \mathrm{SR}_{\boldsymbol{q}}}$, to represent the error of scattering rate calculated by Gaussian broadening ($\mathrm{SR}_{\boldsymbol{q}}$) from the tetrahedron method ($\mathrm{SR}^0_{\boldsymbol{q}}$) at each $\boldsymbol{q}$ point along Γ–A, as shown in Fig. 4(b). When $N_1 = 16$, the adaptive method has larger $\varepsilon_{\mathrm{SR}}$ value than the optimized method along Γ–A. By using a denser grid $N_1 = 32$, the $\varepsilon_{\mathrm{SR}}$ curves of two methods becomes closer and scattering rates seem to converge near point A.

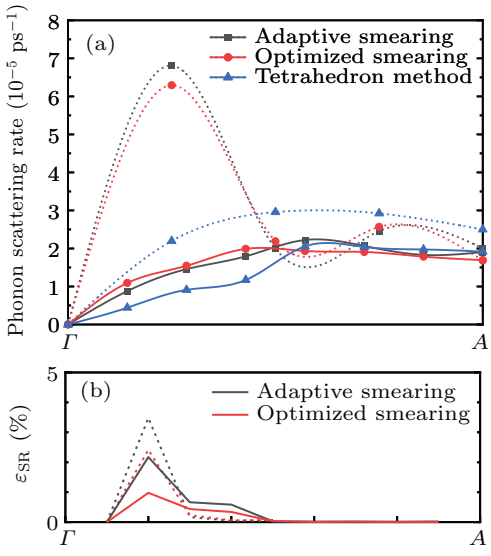


Fig. 4. Comparison of (a) scattering rate of LA phonon along Γ–A axis of three methods and (b) the $\varepsilon_{\mathrm{SR}}$ of two Gaussian function schemes (solid lines of 28×28×14, and dashed lines of 16×16×8).

Although the average error of our scheme and the adaptive scheme is close for the denser grid, we can clearly identify the phonon scattering rate difference for the long-wavelength modes around Γ point. It is also seen that when the wave vector is small, there exists the abnormal fluctuation for the Gaussian function with the denser grid. It is probably due to the fact that the calculated coefficient σ_{A} excessively counts scattering events that should not have occurred for certain phonon modes but insufficiently for other modes. Though our proposed scheme seems to inherit the defects, but the scattering rates of the two neighboring short-wave-vector modes do not deviate from the results of tetrahedron method on average.

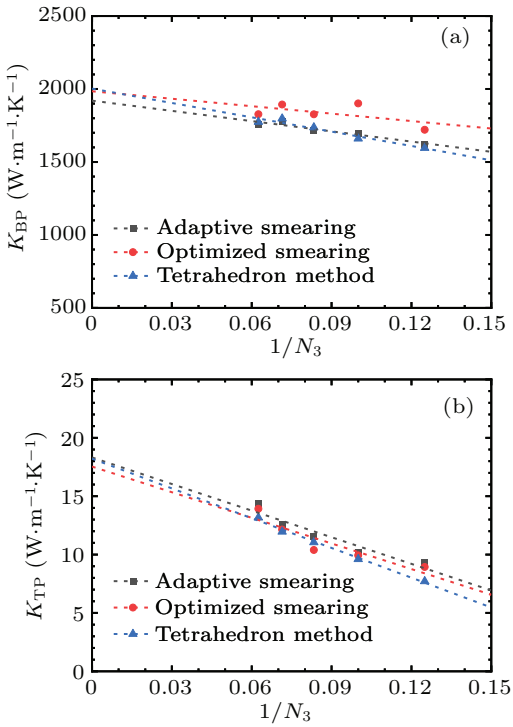


Fig. 5. Thermal conductivity results in (a) basal-plane direction and (b) through-plane direction as a function of the grid density based on three sampling methods in 300 K under the $\boldsymbol{q}$-point grid of $N_1 : N_2 : N_3 = 2 : 2 : 1$.

After analyzing the three-phonon phonon scattering rates, we then show the calculated thermal conductivity as a function of $\boldsymbol{q}$-grid density in Fig. 5. Both the basal- and through-plane thermal conductivities increase with $\boldsymbol{q}$-grid density, which is consistent to previous PBTE studies. To present the results independent of the $\boldsymbol{q}$-grid, the extrapolation is used, in which the relation between the thermal conductivity and the grid density is fitted through $K = K_0 - A/N$, with the fitted slope value A and thermal conductivity K_0 under infinite dense $\boldsymbol{q}$-grid. The rationale of the extrapolation lies in the fact that the long-wavelength acoustic phonons, which are typically capable of conducting heat efficiently, are not included in the coarse grid and thus the computed thermal conductivity is smaller than that from an infinitely dense grid[12] and the existing hardware computing power can only carry out finite density grid sampling. We also believe that if the $\boldsymbol{q}$-grid is dense enough, the thermal conductivity results of different methods will converge to the same value. As seen in Fig. 5(a), all of the three FBZ sampling schemes show that the basal-plane thermal conductivity has similar $\boldsymbol{q}$-grid dependence and converges to $\sim$ 2000 W/m·K when increasing the $\boldsymbol{q}$-grid density to infinite. Meanwhile, the through-plane thermal conductivity, as

shown in Fig. 5(b), also linearly changes with $1/N$ for all of the three sampling methods, and the curves of the three methods evidently converge to $\sim$ 18 W/mK. This observation is consistent with the fact that the scattering rate error value of denser $\boldsymbol{q}$-points on Γ–A in Fig. 4, as on average the scattering rates of phonons along the Γ–A direction are correctly approximated. We also considered the $\boldsymbol{q}$-point grid with a different N_1/N_3 ratio ($N_1 : N_2 : N_3 = 6 : 6 : 1$), which tends to make the energy energy spacing in anisotropic directions closer than that of $N_1/N_3 = 2$. The convergence results obtained using our scheme are almost the same for different N_1/N_3 ratio.

3.2. Sampling methods efficiency comparison

The comparison of the calculated phonon scattering rates and the thermal conductivity along two directions with the tetrahedron method confirms the accuracy of our optimized method. In addition to the accuracy, the computational efficiency is another criterion for evaluation on the FBZ sampling methods. When performing the PBTE calculations, most of the computational burden is devoted to computing the phonon scattering rates, which is related to the amount of scattering events and the specific FBZ integration method. Since our scheme chooses the minimal width of broadening, the Gaussian function along with our scheme could be efficient to compute the scattering rates. Here, we compare the number of three-phonon scattering events of the sampling method in calculating the three-phonon scattering rate under different $\boldsymbol{q}$-point grids shown in Fig. 6(a), which are performed on Intel Xeon CPU Gold 6248@2.5 GHz and 12×16 GB RAM. It is obvious that the overall time consumption of the three methods increases exponentially with denser $\boldsymbol{q}$-point in one direction. The time consumed by Gaussian approximation methods is shorter than the analytical tetrahedron method, which is mainly due to the fact the Gaussian method significantly simplifies the numerical processes by avoiding the procedures of dividing the FBZ and the optimized broadening of Gaussian function effectively filters the number of scattering events. Compared with the adaptive method, our optimized broadening width saves additional 95% of the time consumption on three-phonon scattering rate calculation under 16×16×8 grid.

Due to the heavy computational cost, the effects of four-phonon scatterings on the thermal conductivity of graphite have not been investigated. We compared the numbers of four-phonon scattering events to be calculated by three methods, as shown in Fig. 6(b), where our method demonstrates a significant advantage. In the 12×12×6 grid, our method only needs to calculate 10^5 scattering events for a single phonon mode in 4 hours, while the adaptive method has to compute 3×10^6 events consuming more than 100 hours. Therefore, the proposed smearing scheme can achieve a relatively good computational speed in calculating thermal conductivity, while ensuring accuracy in phonon scattering properties.

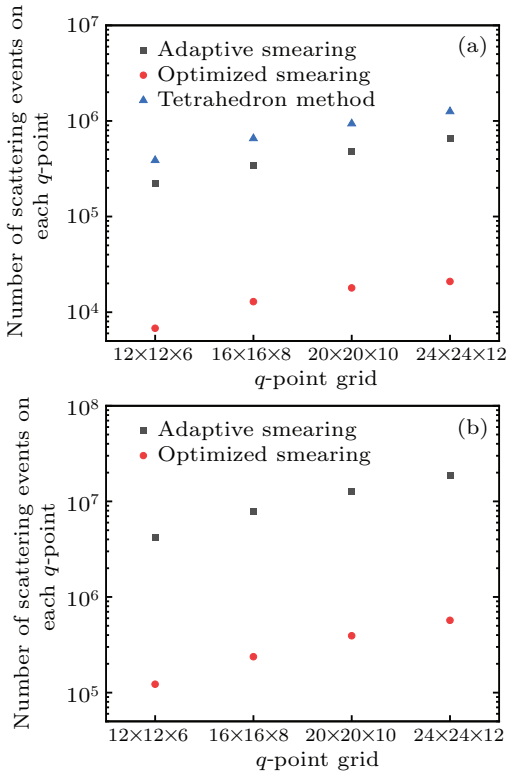


Fig. 6. (a) The number of three-phonon scattering events and (b) the number of four-phonon scattering events compared with the $\boldsymbol{q}$-grid density.

3.3. Influence of four-phonon scatterings on thermal conductivity

Though with our scheme the efficiency of the four-phonon scattering calculation is boosted compared with the other two methods discussed in this work, according to our computational resources we find that only the results using the $\boldsymbol{q}$-grid within 16×16×8 can be obtained within reasonable time (2400 CPU hours). However, as the discussion in Subsection 3.2, one needs to obtain the grid-independent thermal conductivity results based on the results from other denser grids, which is beyond our computational capability. To relieve this issue, we propose two approximation methods. The first one is to determine the four-phonon scattering rates for a $\boldsymbol{q}$-mesh larger than 16×16×8 by interpolating the scattering rates on the 16×16×8 $\boldsymbol{q}$-grid, and then treat four-phonon scattering terms as a purely resistive term

$$W_\lambda^{4\mathrm{ph}} \approx \frac{n_\lambda^0\left(n_\lambda^0+1\right)}{\tau_\lambda^{4\mathrm{ph}}}, \tag{14}$$

where $\tau_\lambda^{4\mathrm{ph}}$ is the relaxation time for mode λ due to four-phonon scatterings, equaling the inverse of the four-phonon scattering rate. With these thermal conductivity results from different $\boldsymbol{q}$-grids, the extrapolated thermal conductivity to an infinite grid can be obtained. In the second method, we compute the three-phonon thermal conductivity $\kappa_{16\times16\times8}^{3\mathrm{ph}}$ and thermal conductivity considering the four-phonon scattering

$\kappa^{3ph+4ph}_{16\times16\times8}$ using the 16×16×8 grid, and then rescale the three-phonon thermal conductivity from other grids by the ratio $\kappa^{3ph+4ph}_{16\times16\times8}/\kappa^{3ph}_{16\times16\times8}$ to obtain the thermal conductivity predictions considering the four-phonon scattering.

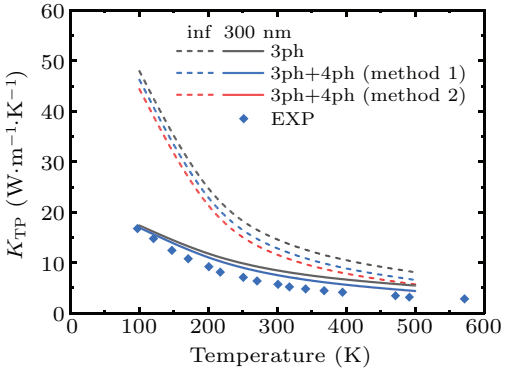


Fig. 7. Thermal conductivity of graphite along the through-plane direction as a function of temperature. The experimental values are from the extrapolation of data in Refs. [30,43].

We compute the thermal conductivity considering the four-phonon scattering using the above mentioned approximation methods, as shown in Fig. 7. The results without including the four-phonon scattering are also plotted as a comparison. Both approximation methods show that four-phonon scattering reduces the thermal conductivity by around 15% in through-plane at 300 K, due to the existence of additional scattering. Figure 8 shows the phonon scattering rate at 300 K. It is seen that the four-phonon scattering rates of LA, TA phonons are about one order of magnitude smaller than the three-phonon ones at 300 K, while low-frequency LO′, TO′ phonons along Γ–A is about two orders of magnitude smaller. For optical phonons, the scattering rates of three-phonon and four-phonon are comparable.

As to the two approximation methods we employ, we find that the predicted degree of thermal conductivity reduction from the two methods have small differences (13.9% vs. 21.5% for through-plane thermal conductivity at 300 K). Despite the consistence of the results from these two approaches, one should be aware that the reported values should be regarded as a lower bound. For the first method, the four-phonon scattering terms included in the scattering term of PBTE as a purely resistive term. However, in reality four-phonon scattering can be classified to non-resistive normal processes and resistive Umklapp processes. The normal processes assist phonons to redistribute to other states, which is beneficial to heat conduction, as more phonons with less capability to conduct heat are converted to other modes. Hence, the predicted results from the first method should be lower than the actual values. For the second method, we determine the percentage of thermal conductivity reduction due to four-phonon scattering through the calculations from a coarse $\boldsymbol{q}$-grid. The small wave-vector phonons are more limited in the coarser grid compared with the denser grids, as a result of which the coarser grid tends to underestimate the role of normal scatterings due to the fact that small wave vector phonons are more likely be scattered through normal processes.

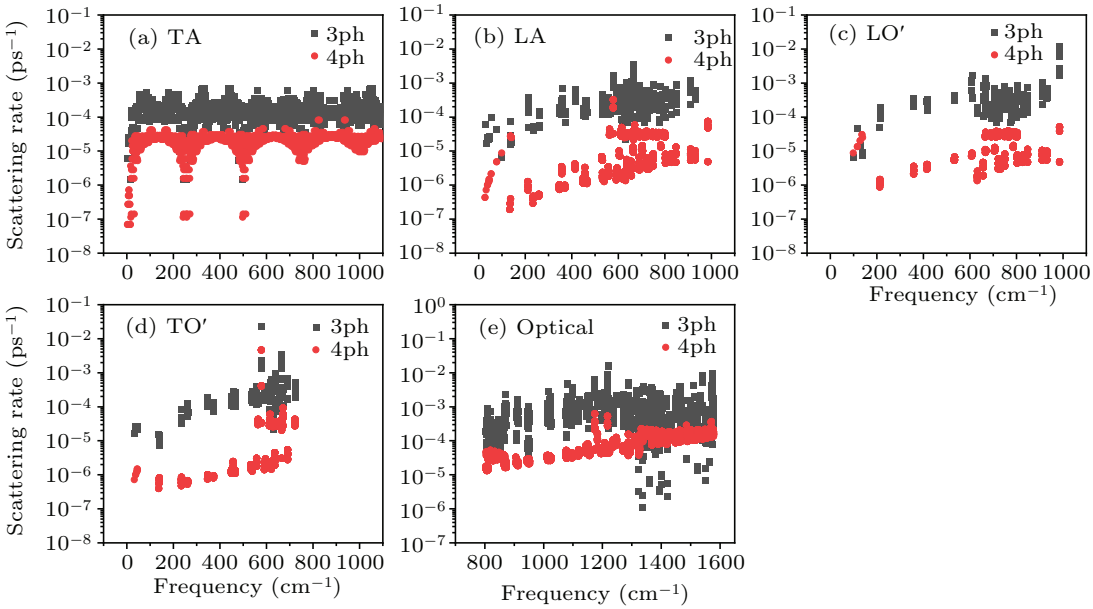


Fig. 8. Comparison of three-phonon and four-phonon scattering rates of phonons on (a) TA, (b) LA, (c) LO′, (d) TO′ branches and (e) optical phonons.

In Fig. 7, we also show the measured thermal conductivity from handbook.[41] It is evident that our predicted through-plane thermal conductivity is higher than the data, even when the four-phonon scattering are included in the calculations. For instance, at 300 K the discrepancy is as large as 5.21 W/mK (10.92 W/mK vs. 5.71 W/mK). Our calculations imply the graphite is a good heat spreader along the through-plane direction, as the thermal conductivity is com-

parable to stainless steel. To understand the discrepancy between the experimental data and our theoretical results, we recall the finding from Zhang *et al.*,[29] where they pointed out that the boundary scattering limits the range of phonon mean free path (MFP) to 40–250 nm reducing the heat conduction, which might be a result of defects per 700–3000 layers (300–800 nm in c-axis) in high-quality graphite sample used in the measurements. To quantitatively characterize the contribution of phonons with different MFP, the cumulative thermal conductivity under 300 K is shown in Fig. 9. Around 90% of the through-plane thermal conductivity is contributed by the phonons of 0–2000 nm and phonons with MFP $<$ 300 nm contribute 3.7 W/mK. To explore the effect of defects on thermal conductivity, we introduce a boundary scattering term[44] in Eq. (2), $W_\lambda^{\text{boundary}} = n_\lambda^0(n_\lambda^0+1)/(L/2v_\lambda^z)$, with the characterizing length scale of between two neighboring defects L and the group velocity along the through-plane direction, and recompute the thermal conductivity, which is also shown in Fig. 7. The thermal conductivity is reduced by 33.3% to 7.28 W/mK compared with ideal sample without defects at room temperature, which is still higher than the experimental result 5.81 W/mK. However, the temperature dependence from our calculation is consistent with the experimental data, indicating our calculation successfully captures the essential scattering mechanisms in graphite. Since the experimental data provided by handbook were obtained by a compilation and analysis of several early research papers, we expect that defect density of the samples in these measurements are quite distinct, as detailed microscopic characterization on atomic structure of graphite samples were not conducted in these early studies. This explains the discrepancy between our theoretical prediction and the measured data. As is known, highly oriented pyrolytic graphite can be classified to different grades, such as ZYA, ZYB and ZYH, depending on the measured mosaic spread. The quality grade reflects the degree of large-scale inplanarity of the carbon layers. It is highly desired to conduct thermal conductivity measurement on graphite samples with different quality grades to establish the connection between thermal conductivity and interlayer defects in graphite and to confirm the high thermal conductivity in perfect defect-free graphite.

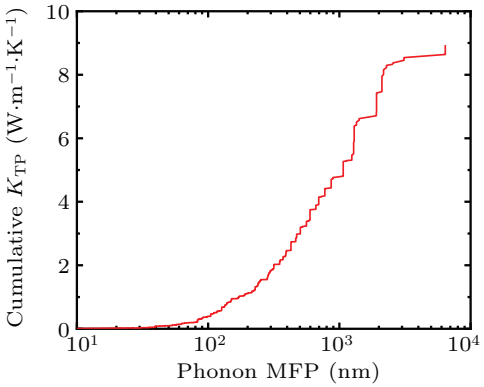


Fig. 9. The MFP changing trend and accumulated thermal conductivity via optimized sampling method under 16×16×8 $\boldsymbol{q}$-grid.

4. Conclusion

To summarize, we derive an optimized smearing scheme for the Gaussian broadening method to perform FBZ sampling, which combines the accuracy of the analytical method with the advantages of the finite-width method for handling phonon branch crossing. The comparison between our scheme and other Brillouin zone sampling methods is presented in Table 2. This proposed method achieves ideal results in calculation speed for both three-phonon and four-phonon scattering rates. We elucidate the phonon scattering errors existing in FBZ high-symmetric point from sampling methods, which results in discrepancy in the predicted values of graphite through-plane thermal conductivity. We further discuss the influence of four-phonon scatterings and boundary scattering on the thermal conductivity of graphite. It is found that four-phonon scatterings reduce the thermal conductivity by around 15% and interlayer defects should be carefully taken into consideration when interpreting the measured through-plane thermal conductivity data in literatures.

Table 2. Comparison of Brillouin zone sampling methods.

Method	Expression of broadening coefficient σ	Evaluation
Fixed broadening	$\sigma =$ constant	It could make phonons experience insufficient scatterings if the σ is too small.
Adaptive broadening	$\sigma = \sqrt{2\sum_\mu \left(\frac{\partial W}{\partial q'^\mu}\right)^2 E\left\{\left(q'^\mu - q'^\mu_0\right)^2\right\}}$	It covers many $\boldsymbol{q}$-points that the energy-conservation condition is not fulfilled when the frequency difference between neighboring $\boldsymbol{q}$ points is highly direction dependent.
Optimized broadening	$\sigma = 0.6\lvert v^\mu\rvert \Delta q^\mu$	The direction with lower average phonon speed is selected as the integration direction and obtain faster calculation efficiency
Tetrahedron smearing		It meets the accuracy but significantly increase the computational burden

Acknowledgements

X. G. acknowledges the support from the National Natural Science Foundation of China (Grant No. 51706134). The computations in this paper were run on the π 2.0 cluster supported by the Center for High Performance Computing at Shanghai Jiao Tong University.

References

[1] Esfarjani K, Garg J and Chen G 2014 *Annu. Rev. Heat Transf.* **17** 9
[2] Lindsay L 2016 *Nanoscale Microscale Thermophys. Eng.* **20** 67
[3] Gu X, Fan Z and Bao H 2021 *J. Appl. Phys.* **130** 210902
[4] Bao H, Chen J, Gu X and Cao B 2018 *ES Energy Environ.* **1** 16
[5] Maradudin A A and Fein A E 1962 *Phys. Rev.* **128** 2589
[6] Tadano T, Gohda Y and Tsuneyuki S 2014 *J. Phys. Condens. Matter* **26** 225402
[7] Chernatynskiy A and Phillpot S R 2015 *Comput. Phys. Commun.* **192** 196
[8] Broido D A, Ward A and Mingo N 2005 *Phys. Rev. B* **72** 014308
[9] Gu X, Fan Z, Bao H and Zhao C Y 2019 *Phys. Rev. B* **100** 064306
[10] Li W, Mingo N, Lindsay L, Broido D A, Stewart D A and Katcho N A 2012 *Phys. Rev. B* **85** 195436
[11] Garg J, Bonini N, Kozinsky B and Marzari N 2011 *Phys. Rev. Lett.* **106** 045901
[12] Esfarjani K, Chen G and Stokes H T 2011 *Phys. Rev. B* **84** 085204
[13] Fugallo G, Lazzeri M, Paulatto L and Mauri F 2013 *Phys. Rev. B* **88** 045430
[14] Blöchl P E, Jepsen O and Andersen O K 1994 *Phys. Rev. B* **49** 16223
[15] Li W, Carrete J, Katcho N A and Mingo N 2014 *Comput. Phys. Commun.* **185** 1747
[16] Lindsay L, Li W, Carrete J, Mingo N, Broido D A, and Reinecke T L 2014 *Phys. Rev. B* **89** 155426
[17] Fei T, Bai S, Xi C, K. R N, Yinchuan L, Ke C, Sean S, Jaehyun K, Yuanyuan Z, Te-Huan L, Miguel G, Zhiwei D, Jingying S, Gamage U G G A, Haoran S, Hamidreza Z, Shuyuan H, Liangzi D, Jianshi Z, J. S A, Shuo C, Ching-Wu C, Y. H P, David B, Li S, Gang C and Zhifeng R 2018 *Science* **361** 582
[18] Sheng L, Qiye Z, Yinchuan L, Xiaoyuan L, Xiqu W, Y. H P, G. C D and Bing L 2018 *Science* **361** 579
[19] Sang K J, Man L, Huan W, Huuduy N and Yongjie H 2018 *Science* **361** 575
[20] Gu X, Li S and Bao H 2020 *Int. J. Heat Mass Transf.* **160** 120165
[21] Feng T and Ruan X 2018 *Phys. Rev. B* **97** 045202
[22] Feng T, Lindsay L and Ruan X 2017 *Phys. Rev. B* **96** 161201(R)
[23] Feng T and Ruan X 2016 *Phys. Rev. B* **93** 045202
[24] Liu H, Qian X, Bao H, Zhao C and Gu X 2021 *J. Phys. Condens. Matter* **33** 405401
[25] Zhang B, Fan Z, Zhao C Y and Gu X 2021 *J. Phys. Condens Matter* **33** 495901
[26] Kelly B T 1967 *Philos. Mag.* **15** 1005
[27] Hooker C N, Ubbelohde A R J P and Young D A 1965 *Proc. R. Soc. London. Ser. A. Math. Phys. Sci.* **284** 17
[28] Wei Z, Yang F, Bi K, Yang J and Chen Y 2019 *Carbon* **144** 109
[29] Zhang H, Chen X, Jho Y D and Minnich A J 2016 *Nano Lett.* **16** 1643
[30] Fugallo G, Cepellotti A, Paulatto L, Lazzeri M, Marzari N and Mauri F 2014 *Nano Lett.* **14** 6109
[31] Paulatto L, Mauri F and Lazzeri M 2013 *Phys. Rev. B* **87** 214303
[32] Fu Q, Yang J, Chen Y, Li D and Xu D 2015 *Appl. Phys. Lett.* **106** 031905
[33] Sun Z, Yuan K, Chang Z, Zhang X, Qin G and Tang D 2019 *J. Appl. Phys.* **126** 125104
[34] Strongman P, Askarpour V and Maassen J 2021 *Phys. Rev. B* **104** 035428
[35] Yates J R, Wang X, Vanderbilt D and Souza I 2007 *Phys. Rev. B* **75** 195121
[36] Giannozzi P, Baroni S, Bonini N, Calandra M, Car R, Cavazzoni C, Ceresoli D, Chiarotti G L, Cococcioni M, Dabo I, Dal Corso A, De Gironcoli S, Fabris S, Fratesi G, Gebauer R, Gerstmann U, Gougoussis C, Kokalj A, Lazzeri M, Martin-Samos L, Marzari N, Mauri F, Mazzarello R, Paolini S, Pasquarello A, Paulatto L, Sbraccia C, Scandolo S, Sclauzero G, Seitsonen A P, Smogunov A, Umari P and Wentzcovitch R M 2009 *J. Phys. Condens Matter* **21** 395502
[37] Lee K, Murray E D, Kong L, Lundqvist B I and Langreth D C 2010 *Phys. Rev. B* **82** 081101(R)
[38] Sabatini R, Küçükbenli E, Pham C H and De Gironcoli S 2016 *Phys. Rev. B* **93** 235120
[39] Wirtz L and Rubio A 2004 *Solid State Commun.* **131** 141
[40] Nicklow R, Wakabayashi N and Smith H G 1972 *Phys. Rev. B* **5** 4951
[41] Mohr M, Maultzsch J, Dobardžić E, Reich S, Milošević I, Damnjanović M, Bosak A, Krisch M and Thomsen C 2007 *Phys. Rev. B* **76** 035439
[42] Maultzsch J, Reich S, Thomsen C, Requardt H and Ordejón P 2004 *Phys. Rev. Lett.* **92** 075501
[43] Ho C Y, Powell R W and Liley P E 1972 *J. Phys. Chem. Ref. Data* **1** 279
[44] Mingo N and Broido D A 2005 *Nano Lett.* **5** 1221